Effects of Frequency and Bandwidth on Diagnostic Information Transfer in Ultrasonic B-Mode Imaging

Craig K. Abbey, Nghia Q. Nguyen, and Michael F. Insana

***Abstract*—Transmitted pressure pulses in ultrasonic B-mode imaging systems are commonly characterized by their center frequency and bandwidth. Both parameters are associated with tradeoffs in spatial resolution and signal-to-noise in ultrasonic system design, with no general understanding of where they are optimal when applied to specific clinical exams. We use the ideal observer and simple psychophysical studies with human observers to evaluate the efficiency of information transfer in B-mode imaging as a function of the transmitted pulse center frequency and fractional bandwidth.**

Our approach uses a statistical model of backscatter relevant to breast imaging, and a 2-D model of pulse propagation based on Rayleigh-Sommerfeld diffraction theory. The statistics of the backscattered signal are combined in an ideal observer calculation that quantifies the task-relevant information contained in the radio-frequency (RF) signal after delay-and-sum beamforming. This is followed by a psychophysical evaluation of observer performance on B-mode envelope-detected images in three simple tasks. This experimental design allows us to track the flow of diagnostic information through RF acquisition and subsequent reading of the envelope image.

In a low-contrast detection task and a high-contrast boundary discrimination task, optimal efficiency for human observers is observed at the highest center frequencies tested (15 MHz) and at moderate bandwidth (40%). For detection of scattering material in a high-contrast hypoechoic lesion, optimal efficiency was observed at lower center frequencies (5 MHz) and higher bandwidth (80%). The ideal observer analysis shows that this task dependence does not arise in the acquisition stage, where efficiency is maximized at 15 MHz with bandwidths of 60% or greater, but rather in the subsequent processing and reading of the envelope image. In addition, at higher frequencies more information is lost in the processing and reading than in the acquisition of reflected signals.

I. Introduction

Ultrasonic B-mode medical imaging systems rely on reflection of a transmitted pulse as the basis for forming an envelope-detected image of the body. The center frequency and bandwidth of the transmitted pulse are known to be important parameters that influence the quality of the resulting image [1], [2]. However, there are often tradeoffs that constrain these parameters. For example, increased center frequency or bandwidth generally leads to higher spatial resolution but may suffer from reduced echo signal-to-noise ratio (eSNR) because of tissue attenuation and acoustic-output constraints that limit the mechanical index of the pulse. It is not generally clear how parameters such as center frequency and bandwidth should be set in the presence of these tradeoffs. In this work, we use an ideal observer approach along with simple human observer studies to evaluate effects of center frequency and bandwidth on B-mode imaging.

Ideally, optimal parameter settings will maximize the transfer of diagnostic information from the body of the patient to the observer reading the image, thereby maximizing diagnostic performance. In this work, the ideal observer methodology [3], [4] is used as a way to quantify the transfer of diagnostic information. The ideal observer is defined as the optimal decision maker for some task of interest given whatever form of data is presented. The ideal observer achieves the highest possible level of performance given the uncertainty in the data. As such, ideal observer methodology can be used to define the efficiency of diagnostic information transfer [5], [6]. An important capability of the ideal observer approach is that it can be applied to various stages in the process of forming the final image. For example, a good acquisition system will efficiently transfer information from the body of the patient to the RF signal. Effective processing of those acquired data will efficiently transfer information to the reader, resulting in improved diagnostic accuracy. Comparing different stages makes it possible to identify where information is lost in a multi-stage process.

The ideal observer approach makes full use of the statistical properties of the data, which makes it problematic to define in clinical images of patients where complete probability density functions are unknown. Therefore, we use a simulation procedure with well-defined statistical properties to investigate simple diagnostic detection and discrimination tasks by the ideal observer as well as human-observer performance studies. The simulation procedure is based on Rayleigh-Sommerfeld diffraction theory [7], [8], which is used to model pulse propagation and reflection in an incoherent scattering medium as a function of the transmitted center frequency and bandwidth. Propagation to the point of focus is used to determine peak rarefactional pressure, which constrains the maximum amplitude of the transmitted pulse according to its mechanical index. Echo signals are beamformed assuming the delay-and-sum method over a sub-aperture, and electronic

Manuscript received December 12, 2011; accepted March 24, 2012. This work was supported in part by the US National Institutes of Health Grant R01-CA118294.

C. K. Abbey is with the Department of Psychology, University of California, Santa Barbara, CA (e-mail: abbey@psych.ucsb.edu).

N. Q. Nguyen and M. F. Insana are with the Departments of Bioengineering and Electrical and Computer Engineering, and The Beckman Institute for Advanced Science and Technology, University of Illinois at Urbana-Champaign, IL.

DOI http://dx.doi.org/10.1109/TUFFC.2012.2302

0885–3010/$25.00 © 2012 IEEE

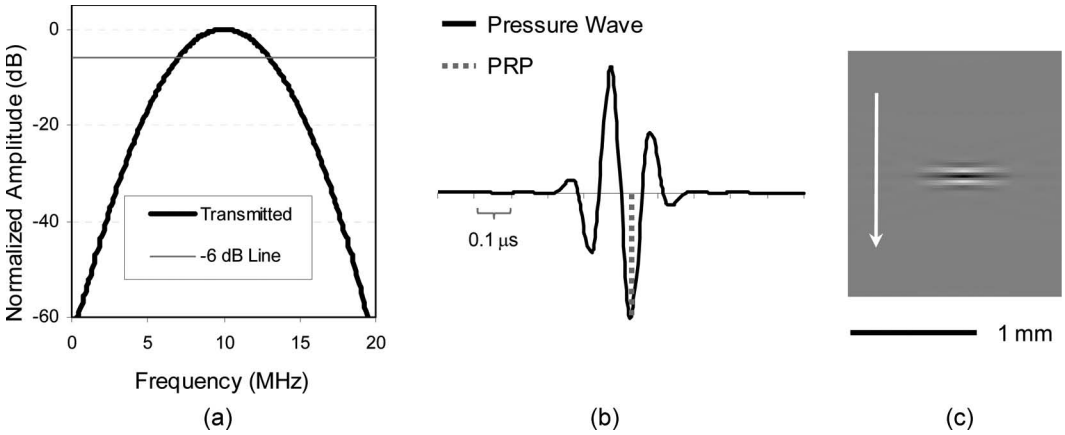

Fig. 1. Components of the pulse-echo model. The Gaussian transmitted pressure amplitude (a) is shown for a 10 MHz, 60% bandwidth pulse. The resulting pressure waveform (b) at a 4-cm focus depth is used to find the peak rarefractional pressure (PRP) for determining the mechanical index. The spatial sensitivity function (c) is shown with a vertical propagation direction (arrow).

acquisition noise is added. We investigate three different classification tasks related to breast sonography used as an adjunct to screening mammography. These include detection of a low-contrast hypoechoic lesion, discrimination of indistinct lesion margins in a high-contrast lesion, and discrimination of an anechoic lesion interior from one with a low-level echo pattern.

Our analysis follows the suggestion of Wagner and Brown [9] and dissects the imaging process into two parts, acquisition and presentation. Acquisition consists of the formation of a beamformed RF signal, whereas presentation refers to the subsequent processing and reading of a B-mode image. Rigorous ideal observers are used to quantify the efficiency of information transfer from the object being imaged to the RF signal. Psychophysical evaluations of reader performance in simple tasks are used to quantify efficiency of information transferred to task performance. In the case of the low-contrast detection task, the approximations of Smith *et al.* [10] allow the construction of an additional ideal observer for the envelope images, thereby isolating this stage of processing.

We evaluate the three tasks across a range of transmit center frequencies (3 to 15 MHz) and fractional bandwidths (20–80%). From a strict end-points perspective, it could be argued that observer performance is the only important performance measure because it characterizes the total performance of the system. However, the ideal observer analysis identifies the points in the process of forming and reading an image at which information is lost, which can be important for understanding and optimizing systems. Taken in sum, the ideal observer analysis and human-observer performance studies reported here demonstrate how information progresses through B-mode imaging systems as a function of the center frequency and bandwidth of the transmitted pulse. In addition, they identify the limiting steps in the imaging process.

II. Theory

In this section we develop a relatively simple model, shown in Fig. 1, for pulse-echo signals in standard B-mode imaging. The underlying framework is Rayleigh-Sommerfeld diffraction theory near the point of focus where Fresnel approximations are valid. The model will be used to evaluate the influence of center frequency and bandwidth on performance in simple tasks using features related to breast cancer detection and malignant/benign discrimination. It is worth noting that more accurate system simulations can be achieved using field II [11], [12] or other acoustic propagation methods [13]. However, we find that this simple model is adequate to isolate the effects of frequency and bandwidth for a generic demonstration of tradeoffs without the many other components of an actual system.

The main purpose of the model is to determine spatial sensitivity profiles to be used in an ideal-observer calculation. The spatial sensitivity profile describes the spatial distribution of field pressure that contributes to the received signal at a given measurement time. An important component of the system is the amplitude of the pulse profile relative to the system noise, as expressed by the eSNR. The model is also used to determine the maximum pulse amplitude allowable, subject to the constraint of an upper bound on the mechanical index. This conforms approximately to regulatory guidelines on linear-array transducers for B-mode imaging, in which mechanical considerations generally limit pulse amplitudes well before thermal limits are of concern [14]–[16].

We will assume a field geometry relative to 1-D linear arrays, in which x represents the lateral direction, y represents the elevational direction, and z represents depth. The transducer face is presumed to lie in the x-y plane at depth $z = 0$ with the center of the transducer at the origin. We denote the focal depth as z_F, and the speed of sound in the medium as $c = 1540$ m/s. For the purposes of this study, involving the tradeoffs in system parameters, we find it sufficient to work in the lateral and axial dimensions, and we will neglect the elevational component.

Rayleigh-Sommerfeld (RS) diffraction theory specifies wave propagation through a complex frequency-dependent spatial field, $\phi_f(x, z)$, derived from a continuous wave set-

ting [8]. The resulting pressure pulse at a position in space is then given by summing together the contributions of all frequencies weighted by the transmitted pressure amplitude, $P_0(f)$. When a point of interest is relatively near the focus and relatively far from the transmission aperture (f-number >1) so that time delays are dominated by the depth, z, the pressure wave is computed as the integral,

$$P(x,z,t) = \mathrm{Re}\Big\{\int \mathrm{d}f\, P_0(f)\phi_f(x,z)e^{-2\pi jtf}\Big\}. \quad (1)$$

We will assume a rectangular transmission aperture of width A_x and height A_y (even though elevation is not explicitly modeled, aperture height still has a scaling effect on the amplitude of the pressure wave). Near the focal region, where Fresnel approximations hold, the spatial field is given by

$$\phi_f(x,z) = \frac{fe^{2\pi j(z/c)f}}{jcz} A_y A_x \,\mathrm{sinc}\Big(\frac{\pi x A_x f}{cz}\Big) 10^{-0.05\alpha f z}, \quad (2)$$

where the final factor represents the effects of attenuation, which we attribute to the spatial field rather than the object function for simplicity. Attenuation in the breast (combining fat and parenchyma) is specified roughly to be $\alpha = 0.75$ dB/cm/MHz [17], [18].

For reasons of computation, it is advantageous to approximate this field under isoplanatic assumptions. These allow us to implement the system model using fast convolution methods that make evaluating the ideal observer much more tractable. We apply these to (2) by approximating z as z_F at all places other than the complex phase factor. The result is the complex spatial field approximated to be

$$\phi_f(x,z) \cong \frac{fe^{2\pi j(z/c)f}}{jcz_F} A_y A_x \,\mathrm{sinc}\Big(\frac{\pi x A_x f}{cz_F}\Big) 10^{-0.05\alpha f z_F}. \quad (3)$$

A. Pulse Parameterization

The parameters of interest for this study (frequency and bandwidth) are embedded in the transmitted pressure amplitude, $P_0(f)$. These will generally be lower than the frequency and bandwidth of a system's driving voltage, which is modulated by the transducer before inducing a pressure wave. We model the pressure amplitude as a Gaussian band in frequency, parameterized by the center frequency, f_c, the fractional bandwidth, B_F, and a constant pressure density, P_{Mag}, that controls the overall amplitude of the pulse. The fractional bandwidth is defined as the full-width at half-maximum (FWHM; −6-dB range) of the transmitted pulse divided by its center frequency. For a Gaussian pulse amplitude, this results in a scaling constant of

$$a = \frac{B_F f_c}{\sqrt{8\ln(2)}}. \quad (4)$$

The transmitted pressure amplitude is then given by

$$P_0(f) = P_{\mathrm{Mag}}\big(e^{-1/2[(f-f_c)/a]^2} + e^{-1/2[(f+f_c)/a]^2}\big), \quad (5)$$

which includes contributions in both positive and negative frequency bands. An example of the pressure amplitude for $f_c = 10$ MHz and $B_F = 60\%$ is shown in Fig. 1(a).

B. Mechanical Limit on Pulse Amplitude

The maximum allowable pulse amplitude in medical ultrasound is limited by mechanical and thermal considerations as defined by regulatory agencies such as the US Food and Drug Administration (FDA) [14]–[16]. However, for scanned linear arrays imaging soft tissue, mechanical limits are generally reached before thermal limits. Hence we will only evaluate a mechanical limit here.

We compute the mechanical index (MI) as the ratio of the peak rarefactional pressure [see Fig. 1(b)] of the transmitted beam in attenuating tissue divided by the square-root of the transmitted center frequency. This is meant to approximate the FDA regulatory guideline, which specifies that peak rarefactional pressure be measured in water, and then derated by 0.3 dB/cm·MHz to account for tissue attenuation. Let z_F be the depth of focus (4 cm in these experiments),

$$\mathrm{MI} = \frac{\max_t(P_{\mathrm{Ambient}} - P(0,z_F,t))}{\sqrt{f_c}}, \quad (6)$$

where P_{Ambient} is the ambient pressure of the medium. MI must be 1.9 or less according to stipulations of the US FDA [14]–[16]. Note that (6) uses the nominal transmitted center frequency in the denominator, even though attenuation will reduce the center frequency somewhat by the time a pulse reaches focus. We choose this because center frequency measurements are typically made in water where there is relatively little attenuation. The pressure amplitude, P_{Mag}, in (5) is set to its maximum value by adjusting it so that MI = 1.9.

C. The Spatial Sensitivity Function

We consider a delay-and-sum beamformer, where the principle of reciprocity holds, resulting in a squaring of the transmitted field [8]. We will also model the frequency dependence of backscatter as part of the spatial sensitivity function (SSF) even though—like attenuation—it is actually a property of the medium. We follow previous literature [19]–[21] and model the backscattered pressure signal as a power law with an exponent of 1.3. The resulting spatial field is given by

$$\psi_f(x,z) = \phi_f(x,z)^2 f^{1.3}. \quad (7)$$

Note that we do not include a scaling constant for the backscatter power law because this will be absorbed into

the conversion gain described below. The spatio-temporal impulse response function, $h(x,z,t)$, models the contribution of a point, (x,z), to the received time signal at time t over an aperture located at the origin,

$$h(x,z,t) = \mathrm{Re}\Big\{\int \mathrm{d}f\, P_0(f)\psi_f(x,z)e^{-2\pi jtf}\Big\}. \tag{8}$$

Under the iso-planatic assumptions in (3), the SSF can be written

$$h(x,z,t) = \mathrm{Re}\left\{\int \mathrm{d}f\, P_0(f)\left(\frac{A_xA_yf}{jcz_F}\mathrm{sinc}\left(\frac{\pi xA_xf}{cz_F}\right)10^{-0.05\alpha fz_F}\right)^2 \times f^{1.3}e^{-2\pi j(t-2z/c)f}\right\}, \tag{9}$$

in which time and depth only enter through the difference $t-2z/c$. Hence spatial sensitivity can be written as a two-dimensional function:

$$h(x,z,t) = h_{\mathrm{sys}}(x,t-2z/c). \tag{10}$$

Fig. 1(c) shows an example SSF.

Let $\gamma(x,z)$ be the local acoustic impedance mismatch of the object being imaged, which is presumed to be static in time. The received RF backscattered signal, after delay-and-sum beamforming, is modeled as [8]

$$g(t) = G_{\mathrm{C}}\int \mathrm{d}x\mathrm{d}z h_{\mathrm{sys}}(x,t-2z/c)\gamma(x,z) + \varepsilon(t), \tag{11}$$

where G_{C} is a conversion gain from the applied force at the transducer face to an amplified voltage signal, and $\varepsilon(t)$ is electronic acquisition noise. Use of a scalar conversion gain in (11) neglects any frequency dependence in transduction. This choice has been made to most clearly demonstrate the effects of transmit frequency of bandwidth under the assumption of an ideal receiver. The rationale for setting a specific value of the conversion gain is given below.

An image is generated by sampling the received signal over a set of laterally translated sub-apertures. Let $g[m,n]$ represent the mth time sample of the received signal at the nth sub-aperture position (i.e., the sub-aperture is centered at x_n), then

$$g[m,n] = G_{\mathrm{C}}\int \mathrm{d}x\mathrm{d}z h_{\mathrm{sys}}(x-x_n,t_m-2z/c)\gamma(x,z) + \varepsilon[m,n]. \tag{12}$$

Noting that h_{sys} is symmetric in x [i.e., $h_{\mathrm{sys}}(x-x_n,t_m-2z/c) = h_{\mathrm{sys}}(x_n-x,t_m-2z/c)$], we see that image formation is modeled as a noisy convolution with the SSF acting as the convolution kernel [5], [6], [22].

Assuming the integral in (12) can be well approximated by sums over a sampled object, the RF data can be written in matrix-vector notation as

$$\mathbf{g} = \mathbf{H}\boldsymbol{\gamma} + \boldsymbol{\varepsilon}, \tag{13}$$

where $\mathbf{g}$ is a column vector of RF data that includes all time samples (t_m) at all aperture positions (x_n), $\boldsymbol{\gamma}$ is the sampled object, $\mathbf{H}$ is a 2-D convolution matrix consisting of the kernel $G_{\mathrm{C}}h_{\mathrm{sys}}$ evaluated at both the RF coordinates and the object sampling coordinates, and $\boldsymbol{\varepsilon}$ is a column vector of electronic noise. For simplicity, we will take the object sampling coordinates and the RF sampling coordinates to be the same. In this case, the model of RF signal formation becomes

$$g[m,n] \cong G_{\mathrm{C}}\Delta x\Delta z\sum_{m'}\sum_{n'} h_{\mathrm{sys}}(x_{n'}-x_n,t_m-2z_{m'}/c)\gamma(x_{n'},z_{m'}) + \varepsilon[m,n]. \tag{14}$$

Note that the sampling in x is determined by the 0.2 mm spacing between array elements ($\Delta x = 0.2$ mm), and the sampling in z is determined by the 40 MHz sampling rate of the system and the speed of sound ($\Delta z = 0.01925$ mm). An example of the convolution kernel in $\mathbf{H}$ is seen in Fig. 1(c). In practice, the convolution is implemented by discrete Fourier transforms, which implies a non-physical wrap-around effect. However, this problem is minimized by constraining all diagnostic features in the test images to be located in the middle of the region of interest where wrap-around is not an issue [23].

The final step in image formation is the computation of an envelope image. An analytic signal is generated by augmenting the received signal with an imaginary component consisting of the signal's Hilbert transform [24], [25]. The final envelope image, $\mathbf{b}$, is the magnitude of the analytic signal. Because the analytic signal is a linear function of the RF, it can be represented by a complex valued matrix, $\mathbf{A}$, to obtain

$$\mathbf{b} = |\mathbf{A}\mathbf{g}|, \tag{15}$$

where the absolute-value brackets are assumed to hold on an element by element basis. The computation of magnitude is irreversible and therefore causes any loss of information relative to the RF signal.

D. Effects of Pulse Propagation

Some effects of pulse propagation are shown in Fig. 2. A plot of normalized pulse amplitudes in Fig. 2(a) shows how propagation and reflection change the center frequency and, to a smaller degree, the bandwidth of the transmitted pulse. This plot serves as a reminder that the transmission parameters we use to characterize the pulse throughout this work are not necessarily representative of the pulse after propagation and reflection in the medium.

The overall strength of the pulse is determined by the transmission parameters. We will measure pulse strength by the eSNR. We define this as the ratio of the received signal variance due to the pulse (and reflective material in the medium) divided by the variance due to acquisition noise, which is assumed to be a constant for any transmis-

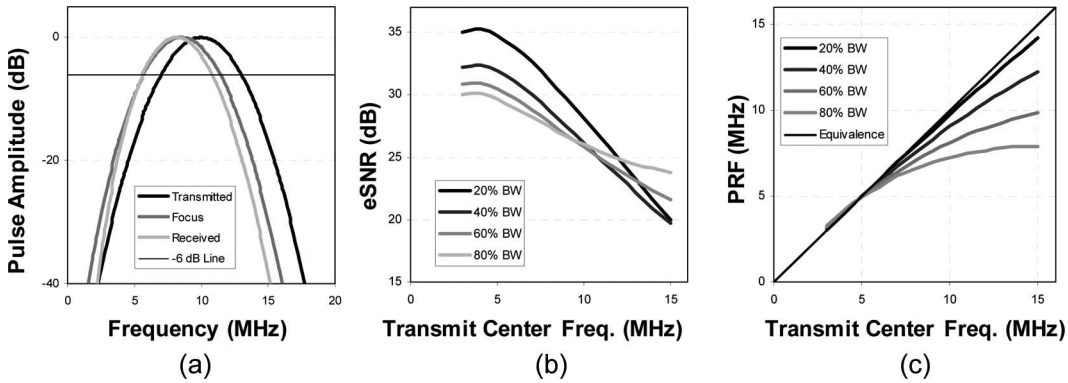

Fig. 2. Propagation effects in the model. The bandwidth plots (a) show pulse amplitudes (normalized to 0 dB) at transmit, focus, and receive. The center frequency of the pulse is 10 MHz, and the fractional bandwidth (BW) is 60% on transmit. The effect of propagation is a reduction in the peak frequency and a slight narrowing of the bandwidth. (b) Echo signal-to-noise ratio (eSNR) drops with frequency because of tissue attenuation, but at a rate dependent on the bandwidth. Frequency-dependent attenuation also reduces the peak received frequency (PRF) of received signals relative to transmit (c), where the peak frequency is equivalent to the pulse center frequency.

sion scheme. To compute the eSNR, we assume that the scattering field, γ in (13), is a white noise process with variance σ_γ^2. The variance due to the reflected pulse is as

$$\sigma_{\text{pulse}}^2 = \sigma_\gamma^2 G_C^2 \int \mathrm{d}x\mathrm{d}z h^2{}_{\text{sys}}(x, 2z/c). \tag{16}$$

Let σ_ε^2 be the variance of the acquisition noise, the eSNR is then defined to be

$$\text{eSNR} = \frac{\sigma_{\text{pulse}}^2}{\sigma_\varepsilon^2}, \tag{17}$$

which is converted to decibels by taking $10\log_{10}$ of the value in (17).

We use the eSNR as a way to determine the conversion gain, G_C, in (11). Laboratory measurement on the Siemens Sonoline Antares system (Siemens Medical Solutions, Mountain View, CA) using uniform scattering media give an eSNR of 30 dB for a 7 MHz pulse at 60% (FWHM) fractional bandwidth [26]. Arbitrarily setting the noise variance and object variance components to unity, we solve for σ_{pulse}^2 in (17), and then solve for G_C in (16). The conversion gain is then fixed across all pulse transmission parameters.

Fig. 2(b) shows the effect of pulse parameters on eSNR. At a 3-MHz transmit center frequency, there is little effect of attenuation on the frequency profile. In this case, the limit on MI allows lower bandwidth pulses to achieve a higher eSNR because they will sum the pulse energy over a greater duration. As the transmit frequency is increased, there is a small initial increase in eSNR due to greater tissue reflectivity [see (7)], but this effect is quickly dominated by attenuation, which leads to a subsequent decrease. However, the effect of bandwidth is reversed at high center frequencies starting at 10 MHz and above. In this case, high fractional bandwidth means that the pulse will contain more low-frequency components that are less affected by attenuation. Frequency-dependent attenuation also explains the reduction in peak received frequency relative to transmit, as seen in Fig. 2(c).

Fig. 2 illustrates the sort of tradeoff that often confronts imaging system designers and users. Simple figures of merit such as eSNR and peak frequency on receive often specify very different system settings for optimality. ESNR favors a low-frequency, low-bandwidth pulse, and peak frequency on receive favors a high-frequency, low-bandwidth pulse. By either of these criteria, there is little reason to consider higher bandwidth signals. As we shall see later in performance assessments, both the ideal observer and human-observer data suggest other settings are optimal.

III. Methods

Our experiments consist of evaluating the effect of the transmitted pulse frequency and bandwidth on task performance (to be defined below). Fig. 3 gives a sense of how these parameters influence the appearance of a simulated hypoechoic lesion. The images shown are all generated from the same scattering object and assume the same realization of electronic noise. Observer experiments were performed on sets of image data consisting of the 20 different combinations of center frequency and fractional bandwidth seen in Fig. 3 in three different tasks described below for a total of 60 different conditions.

A. Defining the Tasks

Three different tasks are evaluated in this work, all having features related to breast cancer detection and malignant/benign discrimination that have been used in previous publications [5], [6]. Each task focuses on a different feature, and therefore the resulting images represent an idealized model of disease that is amenable to simple detection and discrimination tasks. The tasks are as follows: detection of a subtle hypoechoic lesion (Task 1), discriminating a poorly defined lesion boundary from a well circumscribed boundary (Task 3), and discrimination of some scattering matter in a hypoechoic lesion interior

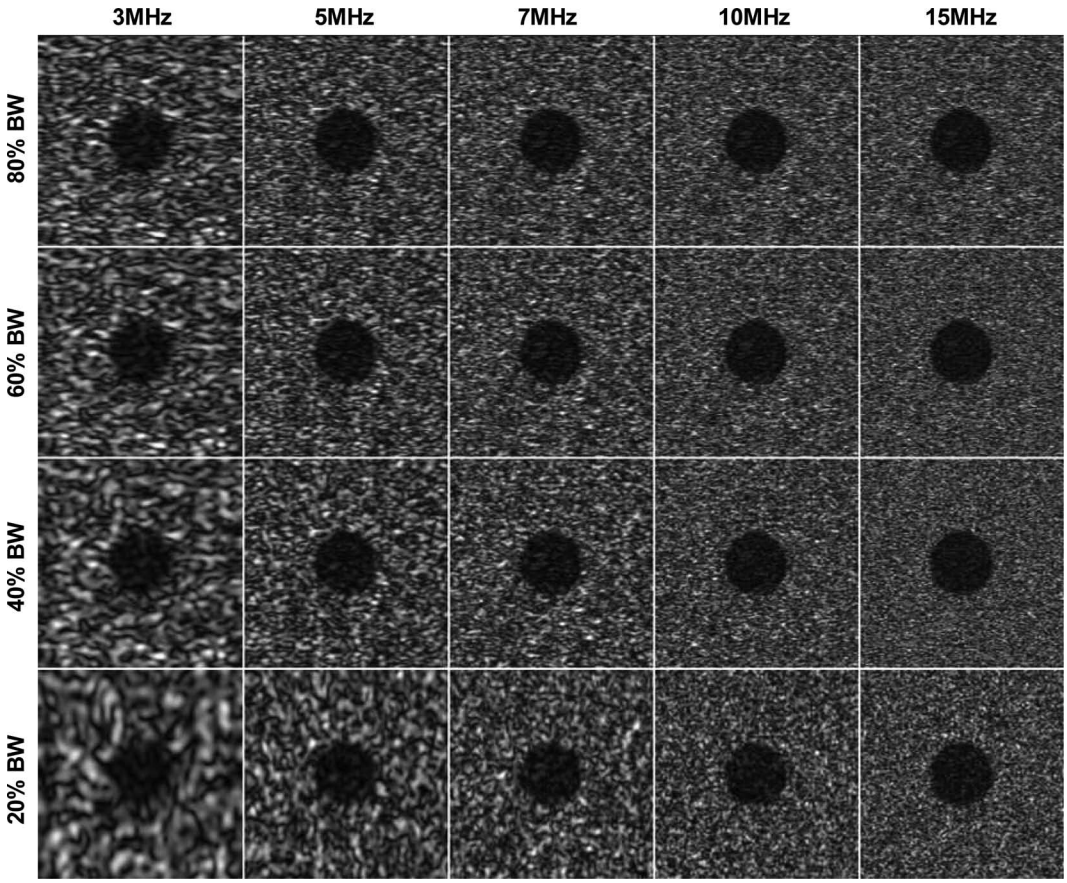

Fig. 3. Example images. Envelope images of a hypoechoic lesion obtained from simulations across the range of transmit frequency and bandwidth (BW) parameters are shown.

(Task 5). In all three tasks, the lesion (when present) is 6 mm in diameter. The task numbers are chosen to correspond with previous studies using these features.

Each task consists of two classes of images representing malignant or benign conditions. Each class is specified by a covariance matrix on the object reflectivity vector, γ, in (13). We will assume that reflectivity of the object being imaged is a Gaussian white-noise process, which corresponds to incoherent scatter generating fully developed image speckle [27]. Specular reflections, which would be implemented as a nonzero mean to the process, are neglected in this work. We will generically denote the benign object covariance matrix (i.e., class 0) of a task as a diagonal matrix, $\sigma_\gamma^2(\mathbf{I}-\mathbf{S}_0)$, where $\mathbf{S}_0$ represents the deviation from a uniform white-noise process. The malignant object covariance matrix (i.e., class 1) is given by the diagonal matrix $\sigma_\gamma^2(\mathbf{I}-\mathbf{S}_1)$. Hence, information for discriminating malignant from benign is contained in the difference between the $\mathbf{S}_0$ and $\mathbf{S}_1$ components of the object covariance matrices. Once the task covariance matrices are determined, an object can be simulated by sampling from the appropriate multivariate Gaussian distribution:

$$\begin{aligned}&\text{Malignant: } \boldsymbol{\gamma} \sim \text{MVN}(\mathbf{0}, \sigma_\gamma^2(\mathbf{I}-\mathbf{S}_1))\\ &\text{Benign: } \boldsymbol{\gamma} \sim \text{MVN}(\mathbf{0}, \sigma_\gamma^2(\mathbf{I}-\mathbf{S}_0)).\end{aligned} \tag{18}$$

Examples of the three tasks considered here are shown in Fig. 4. For Task 1, the benign class is characterized by a uniform scattering field, $\mathbf{S}_0 = 0$. The malignant class is a circular region of lower variance. In this case, $\mathbf{S}_1 = \theta\mathbf{L}$, where the diagonal elements of $\mathbf{L}$ form a circular disk with values of 1 inside a 6 mm diameter at the center of the image. The circular disk is blurred by a Gaussian kernel with a standard deviation of 0.1 mm to reduce pixelation effects in the variance maps. The feature parameter, θ, controls the difficulty of the task. As θ gets larger, the lesion gets more hypoechoic and thus easier to detect. Examples of the two variance maps associated with this task, and example envelope images for a 7-MHz system at 60% fractional bandwidth are shown in Fig. 4(a). For Task 3, the benign class is represented by a strong hypoechoic lesion, $\mathbf{S}_0 = 0.95\mathbf{L}$, whereas the malignant lesion is this profile blurred by a Gaussian kernel. In this case, the feature parameter is the standard deviation (in both x and z directions) of the blurring kernel, and increasing this parameter makes the lesion boundary less distinct and thus easier to discriminate from the sharp boundary of a well-circumscribed benign lesion. If we define the 2-D vector $\mathbf{s}_0$ as the diagonal elements of $\mathbf{S}_0$, then the diagonal elements of $\mathbf{S}_1$ are defined by $\mathbf{s}_1$, where the sharp lesion profile has been blurred through convolution with a Gaussian kernel of width [i.e., $\mathbf{s}_1 = \mathbf{s}_0 * \mathbf{k}(\theta)$, where $\mathbf{k}(\theta)$

is the Gaussian kernel]. Examples of the variance maps and sample envelope images for this task are shown in Fig. 4(b). In Task 5, the benign class is again characterized by a strong hypoechoic lesion ($\mathbf{S}_0 = 0.95\mathbf{L}$). But in this case, the malignant class is represented by more scattering material within the lesion, and thus $\mathbf{S}_1 = (0.95 - \theta)\mathbf{L}$. In this task, increasing θ has the effect of leaving more scattering variance in the lesion, thus making it easier to detect. Fig. 4(c) shows examples of the variance maps for Task 5 with sample envelope images.

The feature parameters have different meanings in the three tasks, but it is helpful to put the differences between classes in all three tasks on a common scale. To do this, we use a definition of object contrast from prior work [5], [6],

$$C = \Delta x \Delta z \sum_n \sum_m |S_1[n,m] - S_0[n,m]|, \tag{19}$$

where $S_1[n,m]$ is the variance map associated with the malignant class, and $S_0[n,m]$ is associated with the benign class. In all three tasks, contrast is monotonically increasing with the feature parameter.

B. The Ideal Observer

We use the concept of the ideal observer, an optimal discriminant function, to measure the information loss between steps in the process. For two-class tasks, the ideal observer is based on the likelihood ratio, log-likelihood ratio, or monotonic equivalents, which can be shown to be optimal under a variety of measures [3], [4], and have been derived previously in the context of ultrasound imaging [5], [6], [23], [28]. In this work, the ideal observer is used at the object stage, the RF acquisition stage, and at the envelope image stage in Task 1. In all cases the effect is to reduce the data set of that particular stage to a decision variable from which performance can be determined, as described below in Section III-C.

Eq. (18) gave the class covariance matrices of the sampled object γ. Under Gaussian assumptions, these can be used to define an equivalent to the log-likelihood ratio test statistic for a particular feature parameter [5],

$$\lambda_{\text{Obj}}(\gamma) = -\frac{1}{2}\gamma^T((\mathbf{I} - \mathbf{S}_1)^{-1} - (\mathbf{I} - \mathbf{S}_0)^{-1})\gamma. \tag{20}$$

Note that the matrix inverses are readily computed because the matrices are diagonal. There are no effects of the SSF here because the object precedes acquisition of an echo signal and is only constrained by the assumed 40 MHz sampling rate.

Linear propagation through the noisy system model in (13) results in a multivariate Gaussian model for the beamformed RF data,

$$\begin{aligned} &\text{Malignant: } \mathbf{g} \sim \text{MVN}(\mathbf{0}, \Sigma_1), \\ &\text{Benign: } \mathbf{g} \sim \text{MVN}(\mathbf{0}, \Sigma_0), \end{aligned} \tag{21}$$

where $\Sigma_i = \sigma_\gamma^2 \mathbf{H}(\mathbf{I} - \mathbf{S}_c)\mathbf{H}^T + \sigma_\varepsilon^2 \mathbf{I}$ is the covariance matrix for class i ($i = 0$ or 1), and σ_ε^2 is the variance of the (white) electronic noise. The log-likelihood ratio for RF signals is similar to the expression for the sampled object [5], [6],

$$\lambda_{\text{RF}}(\mathbf{g}) = -\frac{1}{2}\mathbf{g}^T(\Sigma_1^{-1} - \Sigma_0^{-1})\mathbf{g}. \tag{22}$$

Note that properties of the acquisition system now enter into the ideal observer computation through the class covariance matrices that are dependent on $\mathbf{H}$ and σ_ε.

The covariance matrices in (22) are not diagonal, and are generally non-stationary as well, leaving a potential problem inverting them because of their large size. This problem can be mitigated by using an iterative power-series approach [6]. The power series converges very rapidly for Task 1, where 2 iterations are used, but requires more iterations for Tasks 3 and 5, where 30 or 50 iterations are used, respectively.

Because of the nonlinearity in (15), the statistics of envelope images are more complicated and analytic expressions for their statistical properties are not known [22].

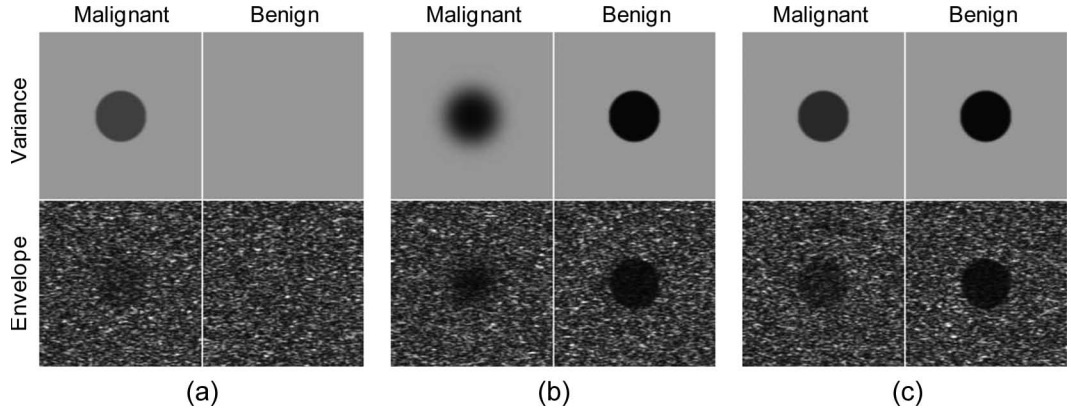

Fig. 4. Discrimination tasks. Examples of the variance maps and sample envelope images for hypoechoic lesion detection (a), discrimination of a less distinct lesion boundary (b), and detection of additional scattering material within the lesion (c). Feature parameters are exaggerated compared with the experiments to facilitate display.

This makes a rigorous derivation of the ideal observer for envelope images difficult. Smith and Wagner [10] derived an approximation to the ideal observer in the limit of low contrast and large area target, which we refer to as the Smith-Wagner (SW) approximation. These conditions are met in Task 1, and hence we use the SW observer to evaluate the effect of generating an envelope image in this task. The SW approximate ideal observer test statistic is

$$\lambda_{\mathrm{SW}}(\mathbf{b}) = -\frac{1}{2}\mathbf{b}^T(\mathbf{S}_1 - \mathbf{S}_0)\mathbf{b}. \tag{23}$$

C. Observer Performance and Efficiency

Monte-Carlo sampling is used to generate random arrays of object reflectivity, as described in (18), and these are used to generate decision variables for the ideal observer at the various stages of image formation. These decision variables are converted into a measure of task performance, the proportion correct denoted P_C, which is equivalent to area under an ROC curve [3], [29]. For a given task (1, 3, or 5) at a given stage (object, RF, or envelope), let λ_j^+ ($j = 1, \ldots, N^+$) generically represent decision variables from the malignant class, and let λ_k^- ($k = 1, \ldots, N^-$) generically represent decision variables from the benign class. Proportion correct is then calculated as

$$P_{\mathrm{C}} = \frac{1}{N^+N^-}\sum_{j=1}^{N^+}\sum_{k=1}^{N^-}\Psi(\lambda_j^+, \lambda_k^-), \tag{24}$$

where Ψ returns 1 if the first argument is greater than the second, 1/2 if the two are equal, and zero otherwise.

The goal of the modeling was to determine the value of the feature parameter leading to a targeted P_{C} of 79.4%. This performance level was chosen to match the threshold in the human-observer studies. Small pilot studies were used to find an approximate threshold, and then a larger study involving 2000 sample images per class was run at the approximate threshold and ±10% of this value. A cumulative Gaussian psychometric function was fit to the three data points, and the threshold value was derived from the fitted curve. This threshold value was converted to contrast according to (19).

For comparing different stages of the imaging process, we use an ideal-observer efficiency measure [5], [6], which is defined as the ratio of squared contrasts at the different stages. For example, the absolute efficiency of the imaging process is defined by comparing the squared contrast threshold of the human observer to that of the ideal observer acting on the object,

$$\eta_{\mathrm{Abs}} = \frac{C_{\mathrm{Obj}}^2}{C_{\mathrm{Hum}}^2}. \tag{25}$$

Because the threshold contrast of the ideal observer at the object stage will always be less than the human observer threshold, up to estimation error, efficiency is confined to the range from zero to one.

Absolute efficiency includes all effects of acquiring a signal, transforming it into an envelope image, and effects of the reader interpreting displayed images. However, it is useful to isolate different steps in this process. For this purpose, relative efficiency measures are used, which consist of the squared-contrast ratio between any two steps in the image formation and decision process. Following work of Wagner and Brown [9], we define an acquisition stage, consisting of the transformation from a sampled object to an RF signal, and a presentation stage, consisting of processing, display, and reading of the image. The absolute efficiency in (25) is the product of both of these relative efficiencies,

$$\eta_{\mathrm{Abs}} = \frac{C_{\mathrm{Obj}}^2}{C_{\mathrm{Hum}}^2} = \frac{C_{\mathrm{Obj}}^2}{C_{\mathrm{RF}}^2}\frac{C_{\mathrm{RF}}^2}{C_{\mathrm{Hum}}^2} = \eta_{\mathrm{Acq}}\eta_{\mathrm{Pres}}. \tag{26}$$

If low absolute efficiency is observed for a given condition, the relative efficiency analysis shows where the information loss is occurring. In Task 1, where the Smith-Wagner assumptions are valid, the relative efficiency of presentation can be further decomposed into envelope and reader components using the SW approximations,

$$\eta_{\mathrm{Pres}} = \frac{C_{\mathrm{RF}}^2}{C_{\mathrm{Hum}}^2} = \frac{C_{\mathrm{RF}}^2}{C_{\mathrm{Env}}^2}\frac{C_{\mathrm{Env}}^2}{C_{\mathrm{Hum}}^2} = \eta_{\mathrm{Env}}\eta_{\mathrm{Hum}}. \tag{27}$$

We note the additional possibility of having human observers perform tasks using the scan-converted RF signal displayed as an image. Informal psychophysical studies (data not shown) suggest that this is a very inefficient mode of display for ultrasound images.

D. Human Observer Studies

All human-observer performance studies were conducted under IRB-approved human-subject protocols at the authors' institutions. Envelope images were evaluated psychophysically using a two-alternative forced-choice adaptive staircase methodology [30], [31]. In each experimental condition, subjects performed a series of forced-choice trials in which two envelope images were presented side by side, as in Fig. 4. Subjects responded by indicating the image from the malignant class. Unlike Fig. 4, the images were randomized so that subjects did not know *a priori* on which side the malignant image appeared. The staircase procedure was based on a commonly used three-up, one-down scheme [31], where the feature parameter remained at the same level until either the subject had three sequential trials correct (the feature parameter was reduced) or the subject made an incorrect decision (the feature parameter was increased). Increases and decreases were 22% relative to the current feature value. Under reasonable assumptions on the smoothness of the underlying psychometric functions, these staircases were designed to

fluctuate about the target threshold at which the observer achieves 79.4% correct responses.

A round of piloting experiments utilizing 100 trials was conducted for each subject to get a rough idea of the threshold in each condition. For each test run, the starting value of the feature parameter in the staircase was double the approximate threshold from the piloting. The first 25 trials of the staircase were considered burn-in trials and were not used in the final threshold estimate. The geometric mean of the feature parameter in the next 75 trials was used as the threshold for the test run, as shown in Fig. 5. The threshold parameters were converted to contrast using (19), and then averaged across the three test runs. The resulting threshold estimates came from a total of 225 trials per subject in each condition.

Subjects performed trials in a darkened room using an LCD clinical review monitor (MDRC 1119, Barco, Kortrijk, Belgium) that was calibrated to the DICOM standard over the luminance range of 0.12 Cd/m^2 to 168.4 Cd/m^2. Calibration and luminance measurements were checked by a spot photometer (Barco). Software for displaying the images and recording subject responses was written by the authors. Subject responses were recorded by capturing a mouse click on the image they decided to classify as malignant. Subjects had unlimited time to view the pair of images in each trial, but typically gave a response after about 1 s. After each trial, feedback was given in the form of text saying "right" or "wrong" displayed for 200 ms.

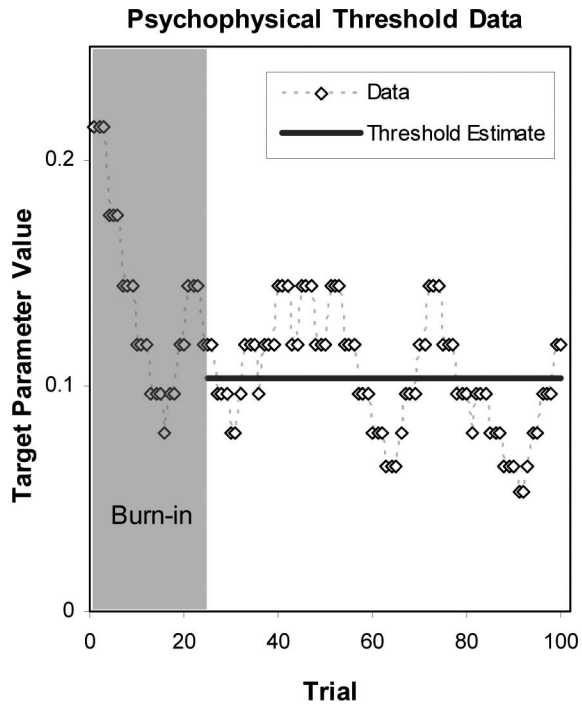

Fig. 5. Staircase psychophysical data. Example data from the 3-up, 1-down staircase procedure are plotted showing how the target parameters vary during a run. The threshold estimate for the run is the geometric mean after 25 trials of burn-in. The average of three such runs is used as the threshold estimate for each observer in each condition.

IV. Results and Discussion

A. Observer Performance

Fig. 6 shows absolute efficiency averaged across 4 subjects with standard errors. Absolute efficiency ranges from 0.2 to 8% across all experiments. Note that an efficiency of 6.5% means that human observers require on average four times the contrast of the ideal observer to achieve equal values of P_c. These results show the settings of center frequency and bandwidth that are optimal for the tasks at hand, up to the limits of statistical inference. Absolute efficiency is generally well below 100%, which suggests that a considerable fraction of diagnostic information is lost in all cases. Relative efficiencies are used below to show where in the process of image formation and reading these losses occur.

Recall from (25) that absolute efficiency consists of the energy threshold of the ideal observer acting on the object ideally sampled on a 0.019-mm interval (corresponding to 40 MHz) to the estimated threshold for human observers of the image data. The sampled-object ideal observer threshold is not concerned with the limitations of an imaging system and is therefore independent of the transmit center frequency or bandwidth. Therefore, C_{obj} is constant within each task, and absolute efficiency is inversely proportional to the threshold contrast energy of the subjects. The sampled-object ideal observer serves to normalize the observed thresholds to a measure of the total diagnostic information incorporated on the human observer's decisions.

In Task 1 and Task 3, absolute efficiency generally increases with center frequency regardless of the bandwidth. The effect of bandwidth changes over the frequency range tested; efficiency steadily increases with bandwidth at the lowest center frequencies (3 MHz), but appears to peak at 40% bandwidth at the highest center frequencies (15 MHz). In Task 5, absolute efficiency appears to peak at approximately 5 MHz for all bandwidths greater than 20%. Thus we find some degree of task dependence in the optimal center frequency and bandwidth settings. However, as noted previously, efficiency is generally low, which motivates the efficiency analysis as a way to understand where diagnostic information is being lost.

B. Efficiency of Information Transfer

Eq. (26) shows how the absolute efficiency plotted in Fig. 6 can be decomposed into relative efficiency measures that track the transfer of information through the acquisition of RF data and the subsequent steps, which we generically refer to as presentation, to a final observer decision. The two panels of plots in Fig. 7 show relative efficiency of acquisition and presentation in each of the three tasks.

In all cases, the relative efficiency of acquisition increases with center frequency regardless of the bandwidth, although the curves appear to flatten somewhat above 10 MHz. Relative efficiency also generally increases with

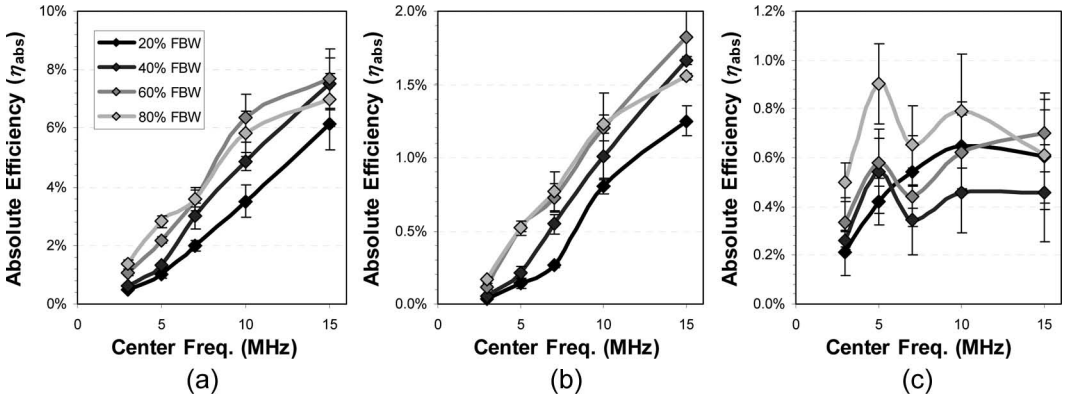

Fig. 6. Absolute efficiency results. Average absolute efficiency across subjects is plotted as a function of the transmit center frequency for each of the 4 tested fractional bandwidths (FBW). Note that the legend in (a) applies to all three graphs. Error bars represent standard errors across subjects.

bandwidth, particularly at low center frequencies. At high center frequencies, higher bandwidth improves relative efficiency up to 60% bandwidth. Note that the relative efficiency of acquisition is computed exclusively from Monte-Carlo simulation studies with the ideal observer using 2,000 sample images, and hence errors are negligible.

A striking feature of these plots is the similarity of performance across the three tasks. From the perspective of the acquisition system, in which the goal is to maximize diagnostic information in a recorded signal, Fig. 7(a) shows that high frequency and high bandwidth are optimal irrespective of the task. This corresponds well with our general intuition about system design, where higher bandwidth and frequency are considered desirable. They also stand in contrast to the optimal echo SNR or peak received frequency shown in Fig. 2.

Fig. 7(b) shows the loss of information resulting from presentation. The plots are not similar across tasks, with flat or mild increases in efficiency with center frequency for Tasks 1 and 3, and a more substantial drop in efficiency for Task 5. The lowest bandwidth (20%) usually exhibits the highest relative efficiency. Thus, some of the bandwidth-related losses in efficiency appear to be made up in the presentation stage. Comparison of the two panels in Fig. 7 shows that the relative efficiency of presentation is often substantially lower than acquisition (note the

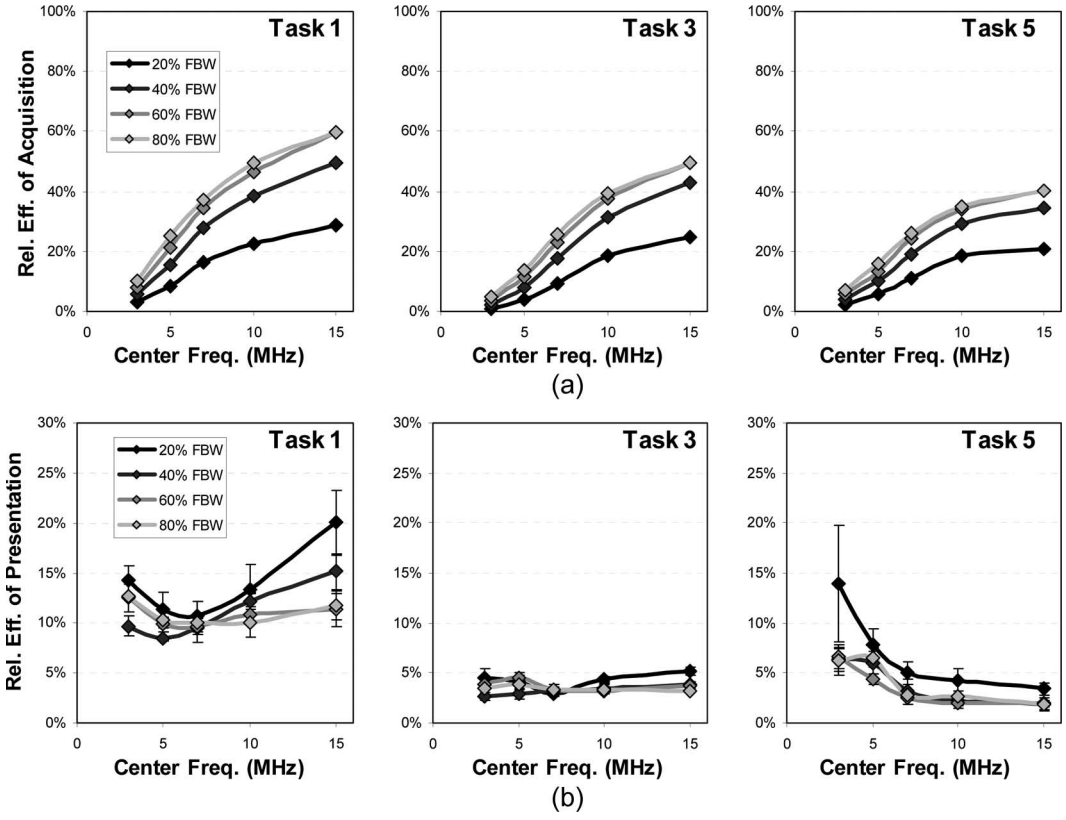

Fig. 7. Information transfer in acquisition and presentation. The upper panel (a) shows the relative efficiency of the RF signal ($\eta_{\text{obj-RF}}$), and the lower panel (b) shows the relative efficiency of the subsequent presentation for each task. The product of the two is the absolute efficiency of Figure 6.

different scales on the y-axis of the plots). Thus, it would appear that in the majority of conditions tested, relatively more information is lost in the conversion to an envelope and subsequent reading of the displayed image than in the acquisition of the RF signal.

As mentioned above, in Task 1 the large-area low-contrast assumptions necessary for the SW approximations are achieved. In this case we can decompose the relative efficiency of presentation into envelope and reader components as described in (27). Plots of these two stages are shown in Fig. 8. The relative efficiency of the envelope images in Fig. 8(a) generally increases with center frequency after an initial dip at 5 MHz. The measure is insensitive to bandwidth until the center frequency is above 10 MHz. At this point the lower bandwidth pulses show substantially higher relative efficiency.

Trends in the relative efficiency of reading in Fig. 8(b) are somewhat the opposite, decreasing with center frequency and dependent on bandwidth across the range of center frequencies. The results suggest that readers are not able to fully capitalize on the increased information available in images acquired with higher frequency and higher bandwidth pulses.

C. Implications

The relative efficiency of acquisition, plotted in Fig. 7(a), shows where further improvements in acquisition may be found. For example, efficiency curves appear to be still increasing at the 15 MHz limit of these experiments, suggesting that higher center frequencies may continue this trend. Furthermore, these results are calculated at an RF echo data sampling rate of 40 MHz. If the sampling rate was increased, the ideal observer acting on the sampled object would likely perform even better, leaving more room for improvement at the level of the RF signal. By contrast, there is less motivation for maintaining high fractional bandwidth at these high frequencies given the observed saturation in performance. It should be noted that this finding may not hold for shallower targets where frequency-dependent attenuation is a smaller factor.

The findings with presentation efficiency show that the single largest relative loss of information occurs after acquisition of an RF signal. This suggests that substantial improvements in imaging may be made without necessarily changing the acquisition hardware at all. In Task 1, where we can assess formation of an envelope image and independent reading of that image, we see that the envelope step loses approximately the same amount of information (relatively) as the reading step. Alternative methods for computing an envelope, for example applying a Wiener filter to the RF signal before demodulation ([5], [6], [23]), may be able to reduce the loss in this step. A possibility for addressing limitations in the observers is task-specific processing of the envelope image.

The study reported here was designed to give a general assessment of frequency and bandwidth effects. However, several specific choices were made regarding the transducer aperture, depth of focus, tissue scattering properties, and other parameters. Furthermore, we neglect effects of aberration, reverberation, focal errors, and tissue-dependent attenuation, which would require fundamental modifications of the transmit-receive model in (11). Although it is possible that other parameter choices could change some of the findings, they also show the broad applicability of the approach.

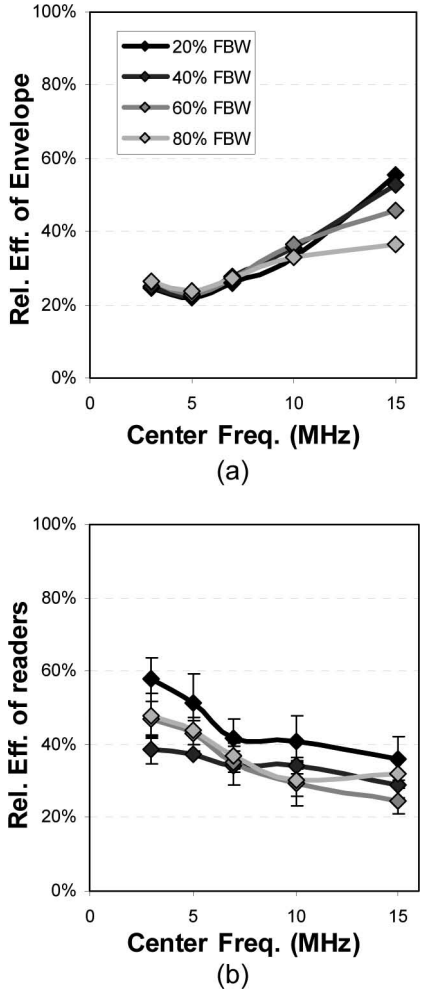

Fig. 8. Envelope analysis of Task 1 using Smith-Wagner (SW) approximations. The SW approximations allow further decomposition of the presentation efficiency into envelope and reader components. At low center frequencies, the relative loss of information is greater in the envelope than the reader, but this situation reverses at high center frequencies. FBW = fractional bandwidth.

V. Conclusions

The purpose of this work has been to investigate the transfer of diagnostic information in B-mode imaging as a function of center frequency and fractional bandwidth of the transmitted pulse. Conventional wisdom would suggest that increasing either of these is beneficial. However, when pulse transmission is subject to a limit on mechanical index, there is a tradeoff between these parameters and the received eSNR. The ideal observer recasts these trad-

eoffs in terms of diagnostic information transfer, which can resolve this ambiguity.

When the entire process of acquisition and presentation is considered, we find the optimal center frequency and bandwidth to be task dependent. High center frequency (15 MHz) and moderately high fractional bandwidth (60%) in a low-contrast detection task (Task 1) and high-contrast boundary discrimination task (Task 3), whereas low center frequency (5 MHz) and high bandwidth (80%) are optimal for a weakly scattering lesion interior task (Task 5). However, when the process is broken into acquisition and presentation stages, we find that the task dependence arises in the presentation stage, suggesting that task-specific processing may resolve this problem rather than task-specific hardware. We also find that the larger proportional loss of diagnostic information is usually found in the presentation stage, particularly as the center frequency exceeds 10 MHz. This suggests that careful processing of high-frequency RF echo signals may lead to even better visual discrimination performance.

We have tried to emphasize the strong constraints and assumptions used to make the comparisons we report. Many of these are not inherent to the ideal observer approach and can be overcome by careful and focused investigations. The ideal observer analysis allows us to better understand the mechanisms that lead to these optimal points. High center frequencies lead to more efficient RF acquisition, and moderate bandwidth allows better transmission of information into the envelope image.

Acknowledgments

This work was supported in part by the U.S. National Institutes of Health Grant R01-CA118294. The authors are grateful to Prof. W. D. O'Brien, Jr., University of Illinois at Urbana-Champaign, for insight into regulatory practice.

References

[1] J. T. Bushberg, J. A. Seibert, E. M. Leidholdt, Jr., and J. M. Boone, *The Essential Physics of Medical Imaging*, 2nd ed. Philadelphia, PA: Lippincott Williams & Wilkins, 2002.

[2] J. A. Zagzebski, *Essentials of Ultrasound Physics*. St. Louis, MO: Mosby, 1996.

[3] H. H. Barrett, C. K. Abbey, and E. Clarkson, "Objective assessment of image quality. III. ROC metrics, ideal observers, and likelihood-generating functions," *J. Opt. Soc. Am. A*, vol. 15, pp. 1520–1535, Jun. 1998.

[4] H. L. Van Trees. *Detection, Estimation, and Modulation Theory*, vol. I. New York, NY: Wiley, 1968.

[5] C. K. Abbey, N. Q. Nguyen, and M. F. Insana, "Optimal beamforming in ultrasound using the ideal observer," *IEEE Trans. Ultrason. Ferroelectr. Freq. Control*, vol. 57, pp. 1782–1796, Aug. 2010.

[6] C. K. Abbey, R. J. Zemp, J. Liu, K. K. Lindfors, and M. F. Insana, "Observer efficiency in discrimination tasks simulating malignant and benign breast lesions imaged with ultrasound," *IEEE Trans. Med. Imaging*, vol. 25, pp. 198–209, Feb. 2006.

[7] J. W. Goodman, *Introduction to Fourier Optics*, 2nd ed. New York, NY: McGraw-Hill, 1996.

[8] K. S. Kim, J. Liu, and M. F. Insana, "Efficient array beam forming by spatial filtering for ultrasound B-mode imaging," *J. Acoust. Soc. Am.*, vol. 120, pp. 852–861, Aug. 2006.

[9] R. F. Wagner and G. G. Brown, "Unified SNR analysis of medical imaging systems," *Phys. Med. Biol.*, vol. 30, no. 6, pp. 489–518, 1985.

[10] S. W. Smith, R. F. Wagner, J. M. Sandrik, and H. Lopez, "Low contrast detectability and contrast/detail analysis in medical ultrasound," *IEEE Trans. Sonics Ultrason.*, vol. 30, no. 3, pp. 164–173, 1983.

[11] J. A. Jensen, "Field: A program for simulating ultrasound systems," *Med. Biol. Eng. Comput.*, vol. 34, suppl. 1, pt. 1, pp. 351–353, 1996.

[12] J. A. Jensen and N. B. Svendsen, "Calculation of pressure fields from arbitrarily shaped, apodized, and excited ultrasound transducers," *IEEE Trans. Ultrason. Ferroelectr. Freq. Control*, vol. 39, no. 2, pp. 262–267, 1992.

[13] X. Zeng and R. J. McGough, "Evaluation of the angular spectrum approach for simulations of near-field pressures," *J. Acoust. Soc. Am.*, vol. 123, pp. 68–76, Jan. 2008.

[14] *Biological Evaluation of Medical Devices Part 1: Evaluation and Testing*, ISO-10993–1, 2003.

[15] NCRP, "Exposure criteria for medical diagnostic ultrasound: II. Criteria based on all known mechanisms," National Council on Radiation Protection and Measurements, Bethesda, MD, NCRP Report No. 140. 2002.

[16] US FDA, "Information for manufacturers seeking marketing clearance of diagnostic ultrasound systems and transducers," U.S. Food and Drug Administration, Silver Spring, MD, 2008.

[17] M. O. Culjat, D. Goldenberg, P. Tewari, and R. S. Singh, "A review of tissue substitutes for ultrasound imaging," *Ultrasound Med. Biol.*, vol. 36, pp. 861–873, Jun. 2010.

[18] ICRU, "Tissue substitutes, phantoms, and computational modelling in medical ultrasound," International Commission on Radiation Units and Measurements, Bethesda, MD, 1998.

[19] M. E. Anderson, M. S. Soo, and G. E. Trahey, "In vivo breast tissue backscatter measurements with 7.5- and 10-MHz transducers," *Ultrasound Med. Biol.*, vol. 27, pp. 75–81, Jan. 2001.

[20] F. T. D'Astous and F. S. Foster, "Frequency dependence of ultrasound attenuation and backscatter in breast tissue," *Ultrasound Med. Biol.*, vol. 12, pp. 795–808, Oct. 1986.

[21] K. A. Wear, T. A. Stiles, G. R. Frank, E. L. Madsen, F. Cheng, E. J. Feleppa, C. S. Hall, B. S. Kim, P. Lee, W. D. O'Brien Jr., M. L. Oelze, B. I. Raju, K. K. Shung, T. A. Wilson, and J. R. Yuan, "Interlaboratory comparison of ultrasonic backscatter coefficient measurements from 2 to 9 MHz," *J. Ultrasound Med.*, vol. 24, pp. 1235–1250, Sep. 2005.

[22] R. J. Zemp, C. K. Abbey, and M. F. Insana, "Linear system models for ultrasonic imaging: application to signal statistics," *IEEE Trans. Ultrason. Ferroelectr. Freq. Control*, vol. 50, pp. 642–654, Jun. 2003.

[23] N. Q. Nguyen, C. K. Abbey, and M. F. Insana, "An adaptive filter to approximate the Bayesian strategy for sonographic beamforming," *IEEE Trans. Med. Imaging*, vol. 30, pp. 28–37, Jan. 2011.

[24] R. N. McDonough and A. D. Whalen, *Detection of Signals in Noise*, 2nd ed. San Diego, CA: Academic Press, 1995.

[25] H. Urkowitz, *Signal Theory and Random Processes*. Dedham, MA: Artech House, 1983.

[26] S. S. Brunke, M. F. Insana, J. J. Dahl, C. Hansen, M. Ashfaq, and H. Ermert, "An ultrasound research interface for a clinical system," *IEEE Trans. Ultrason. Ferroelectr. Freq. Control*, vol. 54, pp. 198–210, Jan. 2007.

[27] R. F. Wagner, M. F. Insana, and S. W. Smith, "Fundamental correlation lengths of coherent speckle in medical ultrasonic images," *IEEE Trans. Ultrason. Ferroelectr. Freq. Control*, vol. 35, no. 1, pp. 34–44, 1988.

[28] R. J. Zemp, M. D. Parry, C. K. Abbey, and M. F. Insana, "Detection performance theory for ultrasound imaging systems," *IEEE Trans. Med. Imaging*, vol. 24, pp. 300–310, Mar. 2005.

[29] D. M. Green and J. A. Swets, *Signal Detection Theory and Psychophysics*. New York, NY: Wiley, 1966.

[30] M. A. García-Pérez, "Forced-choice staircases with fixed step sizes: Asymptotic and small-sample properties," *Vision Res.*, vol. 38, pp. 1861–1881, Jun. 1998.

[31] M. R. Leek, "Adaptive procedures in psychophysical research," *Percept. Psychophys.*, vol. 63, pp. 1279–1292, Nov. 2001.

Authors' photographs and bios were unavailable at time of publication.